

Flame Propagation on the Surfaces of Rapidly Rotating Neutron Stars during Type I X-ray Bursts

Yuri Cavecchi^{1,2*}, Anna L. Watts¹, Jonathan Braithwaite³, Yuri Levin^{4,2}

¹*Astronomical Institute “Anton Pannekoek”, University of Amsterdam, Postbus 94249, 1090 GE Amsterdam, The Netherlands*

²*Sterrewacht Leiden, University of Leiden, Niels Bohrweg 2, NL-2333 CA Leiden, The Netherlands*

³*Argelander Institut für Astronomie, Universität Bonn, Auf dem Hügel 71, 53121 Bonn, Germany*

⁴*Monash Center for Astrophysics and School of Physics, Monash University, Clayton, VIC 3800, Australia*

October 22, 2021

ABSTRACT

We present the first vertically resolved hydrodynamic simulations of a laterally propagating, deflagrating flame in the thin helium ocean of a rotating accreting neutron star. We use a new hydrodynamics solver tailored to deal with the large discrepancy in horizontal and vertical length scales typical of neutron star oceans, and which filters out sound waves that would otherwise limit our timesteps. We find that the flame moves horizontally with velocities of the order of 10^5 cm s⁻¹, crossing the ocean in a few seconds, broadly consistent with the rise times of Type I X-ray bursts. We address the open question of what drives flame propagation, and find that heat is transported from burning to unburnt fuel by a combination of top-to-bottom conduction and mixing driven by a baroclinic instability. The speed of the flame propagation is therefore a sensitive function of the ocean conductivity and spin: we explore this dependence for an astrophysically relevant range of parameters and find that in general flame propagation is faster for slower rotation and higher conductivity.

Key words: stars: neutron, X-rays: bursts, hydrodynamics, methods: numerical

1 INTRODUCTION

Type I bursts are tremendous thermonuclear explosions on the surface of accreting neutron stars (NSs), with luminosities that can easily reach the Eddington limit. They are characterized by a fast increase in the X-ray luminosity, known as the rise, that lasts from less than a few seconds up to tens of seconds, and by an exponential, slow decay, the tail, that lasts from tens of seconds to a few minutes (Lewin et al. 1993; Galloway et al. 2008). More than 90 known X-ray sources have shown Type I bursts (for an up-to-date list see In’t Zand web page <http://www.sron.nl/~jeanz/bursterlist.html>). All are low mass X-ray binaries, where the NS accretes matter from the outer layers of the companion.

Whether the accreted fluid spreads freely or is confined to part of the NS surface probably depends on whether the accretion takes place via a boundary layer (the disc directly ‘touching’ the NS, Inogamov & Sunyaev 2010) or via magnetic channelling and, subsequently, on the strength of the magnetic field itself (Brown & Bildsten 1998). The majority of bursters do not show persistent pulsations, while those that do feature very weak magnetic fields. It is therefore reasonable to assume that the accreted material spreads over all of the NS surface, forming a thin highly combustible ocean consisting of mostly light elements.

As new fluid piles up, the deeper layers are compressed until the temperature and density are high enough to trigger nuclear reactions of H, He or both. Depending on the accretion rate and the composition of the fluid, the burning can be stable or unstable (Fujimoto et al. 1981): in the latter case Type I bursts occur. It seems unlikely that the whole star ignites at the very same moment (Shara 1982); instead it is more likely that the ocean ignites locally and that the resulting flame propagates laterally and engulfs the whole (or a substantial fraction) of the NS surface. It is the physics of the lateral propagation of the thermonuclear flame that is the focus of this study. Our goal is to investigate the open question of what controls the propagation of the flame and the ignition of unburnt fuel. Mechanisms that may be involved include conduction, turbulent mixing associated with convection or other hydrodynamical instabilities, or compression (of unburnt fuel by elements that are already burning and hence expanding). Answering this question is critical to explaining burst time scales, such as the rise times. It is also relevant to the development of burst oscillations (fluctuations in the intensity of the burst lightcurves, see Watts 2012 for a review). The mechanisms suggested to explain such oscillations always involve some kind of asymmetry on the burning surface, such as the presence of a hot-spot (Strohmayer et al. 1996) or surface mode patterns excited by the flame (Heyl 2004; Piro & Bildsten 2005; Berkhout & Levin 2008). Spitkovsky et al. (2002, hereafter SLU) suggested that the Coriolis force might confine burning material in ‘thermonuclear hurricanes’, pointing out the importance of

* E-mail: ycavecchi@uva.nl

the rotation of the star and of hydrodynamics for the flame propagation.

Early attempts at multi-dimensional simulations of the flame propagation mechanism include Nozakura et al. (1984), who followed a zonal approach, and Fryxell & Woosley (1982a), who hydrodynamically simulated the first few milliseconds of a detonation in a thick layer. Zingale et al. (2001) continued this line of research, following the detonating flame for up to hundreds of milliseconds. However the thick layers required for detonation are unlikely to accumulate between bursts, so that in reality the flame probably develops via deflagration (Malone et al. 2011). The most recent studies of flame propagation, which last again only a few milliseconds (far shorter than the timescales of real X-ray bursts), are those by Simonenko et al. (2012a,b). In the first of these papers, the flame propagates via a detonation wave, in a manner similar to that in Zingale et al. (2001). The authors find that propagation is due to the hot fluid expanding and spilling over the top of the cold fluid, which then compresses and ignites. In the second paper, the authors explore regimes with densities $\sim 2 \times 10^7 \text{g/cm}^3$ at the base of the ocean, conditions where one might expect deflagration rather than detonation. However, in this case the simulations did not develop a steadily propagating flame.

None of these studies, however, took into account the rotation of the NS. SLU studied the role of the Coriolis force in flame dynamics and concluded that the Rossby adjustment radius (the horizontal length scale over which the Coriolis force becomes effective in laterally confining the high or low-pressure region) may determine the horizontal scale of the burning front. They also pointed out the importance of the ageostrophic flow¹ at the hot-cold fluid interface as part of the mechanism for the flame propagation itself. That said, SLU used a two layer, shallow water, method to simulate the propagation of the flame and therefore had to make phenomenological assumptions about heat and momentum transport in the vertical direction. Our simulations do not involve such assumptions, and are resolved in the vertical direction, allowing us to make a detailed study of the flame-propagation physics, taking full account of rotation.

In this paper, we simulate flame propagation on a domain that has a horizontal extent that is a substantial fraction of the surface of the NS. At the heart of our simulations is the hydrodynamical code described in Braithwaite & Cavecchi (2012, hereafter BC). It is a multidimensional code, which, by construction, enforces hydrostatic equilibrium in the vertical direction (this assumption is justified since the timescale for sound propagation in the vertical direction in the burning layer is much shorter than the nuclear reaction timescale). Hydrostatic equilibrium allows us to use a longer time step, which would otherwise be limited by sound wave propagation in the vertical direction.

There are other methods that remove sound waves: adopting an implicit scheme is one efficient way, or one can use the basic constant-density incompressible approximation (in which sound and buoyancy waves are both absent), the anelastic approximation (Ogura & Phillips 1962) or the Boussinesq approximation (see Lilly 1996 for a review). These latter approximations can be used under the assumptions that the thermodynamic variables are close to a hydrostatically balanced background state, that the frequency

of the motions is much less than the frequency of sound waves and that the vertical to horizontal length scale ratio or the motion is not too large. However, the hydrostatic approximation also allows us to use *pressure as the vertical coordinate*. This is a great advantage, because we can follow the inflation of the fluid without the need for extra grid points which would lie unused for most of the simulation, consuming extra memory and increasing calculation time (for more details see BC).

In Sec. 2 we briefly review the numerical code described in BC and introduce the additions and modifications made to the code in order to study thermonuclear flame propagation. We then report our results on flame spreading in Sec. 3. We focus in particular on the mechanisms that drive flame propagation and investigate the speed dependence on the rotation rate and conductivity. We conclude with a brief summary in Sec. 4.

2 NUMERICAL IMPLEMENTATION

In this section we describe the modifications made to the code reported by BC in order to make it suitable for study of flame propagation during Type I X-ray bursts. First however we briefly review the most salient features of the code as outlined in BC. It is a 3D magnetohydrodynamical code, which uses the σ -coordinate system (a pressure coordinate system, see below) on a staggered grid: thermodynamical variables such as temperature, pressure, density and heat sources are evaluated at the centres of the grid cells, while velocities are evaluated on the “faces” of the cells. The code is 3D, but for this paper we use a 2D version, assuming that variables are independent of one of the horizontal dimensions. We also neglect magnetic fields, postponing this for future research.

The assumption of vertical hydrostatic equilibrium, justified by the short vertical sound crossing time (much shorter than any time scale of interest in burst simulations), allows us to discard vertically propagating sound waves, numerical resolution of which consumed the lion’s share of the CPU time in previous numerical experiments. In our simulations we can therefore employ much longer timesteps than previous studies. Vertical equilibrium leads naturally to the introduction of a vertical pressure coordinate. This in turn makes it possible to follow the fluid as it expands, without the need for extra grid cells.

The code evolves the two horizontal components of the fluid velocity, the pressure (which acts as a pseudo density) and the temperature using a three step Runge-Kutta scheme, while the spatial derivatives are calculated with sixth-order finite differences. Pressure is defined as

$$P = \sigma P_* + P_T \quad (1)$$

where $P_* = P_B - P_T$ and P_B and P_T are the pressure at the bottom and at the top of the simulation. P_T is a constant parameter in the simulations and $\sigma \in [0, 1]$ becomes the vertical coordinate (0 corresponding to the top and 1 to the bottom). P_* can be shown to become a pseudo density and the continuity equation becomes

$$\frac{\partial P_*}{\partial t} = -I_{\sigma=1} \quad (2)$$

where

$$I \equiv \int_0^\sigma \nabla_\sigma \cdot (P_* \mathbf{u}) \, d\sigma', \quad (3)$$

\mathbf{u} being the horizontal component velocity and $\nabla_\sigma = \hat{\mathbf{x}}\partial_x + \hat{\mathbf{y}}\partial_y$, taken at constant σ .

¹ A geostrophic flow is a general configuration in which the pressure forces are exactly balanced by the Coriolis force: $\nabla P = 2\rho\boldsymbol{\Omega} \times \mathbf{u}$. The fluid motion is along the surfaces of constant pressure (see Pedlosky 1987). In an ageostrophic flow this condition does not hold.

Defining the Lagrangian derivative as $D/Dt = \partial_t + u_x \partial_x + u_y \partial_y + \dot{\sigma} \partial_\sigma$, the momentum and energy equations are

$$\frac{D\mathbf{u}}{Dt} = -\nabla_\sigma \phi - \sigma \frac{\nabla P_*}{\rho} - 2\boldsymbol{\Omega} \times \mathbf{u} + \mathbf{F}_{\text{visc}}. \quad (4)$$

$$c_P \frac{DT}{Dt} = \frac{1}{\rho} \frac{DP}{Dt} + Q, \quad (5)$$

where

$$\phi = gz = P_* \int_{\sigma}^1 \frac{d\sigma'}{\rho}, \quad (6)$$

ρ is the density, $\boldsymbol{\Omega}$ is the rotation vector of the star, parallel to the z direction, \mathbf{F}_{visc} are the viscous forces, c_P is the heat capacity at constant pressure and Q is the heat per unit mass per unit time (see BC for more details); the equation of state (EOS) in BC is a perfect monoatomic gas.

We now move on to discuss the modifications to the code that were implemented to render it suitable for Type I burst simulations.

2.1 Equation of state

The first relevant change is to the EOS for the fluid in our simulations, which has to be able to describe the physics of the NS ocean. We take into account the composition of the fluid by expressing it in terms of the mass fraction: X is the fractional mass of H, Y that of He and $Z = 1 - X - Y$ the fraction of all heavier elements. For a fully ionized perfect gas, the perfect gas EOS used in BC becomes (assuming full ionization):

$$P = \frac{\rho RT}{\mu} \quad (7)$$

with

$$\mu = \frac{12}{7 + 17X + 2Y} \text{ g mol}^{-1}. \quad (8)$$

However, since conditions in the NS ocean can lead to electron degeneracy, which plays an important role in the vertical support of the ocean against the gravitational field, we must take this into account in our simulations. We still consider the atoms to be fully ionized; however whilst the nuclei are assumed to be a perfect gas, the electrons may be (partially) degenerate and (partially) relativistic. We also need to include radiation pressure.

For this purpose we adapted the publicly available routine `helmeos`² of Timmes & Swesty (2000). It uses the density ρ , temperature, X and Y to derive pressure, energy, the thermodynamic potentials and their derivatives with respect to ρ , T , X and Y . In our code structure ρ is a derived quantity, while pressure is a primary quantity (see BC, sec. 2). To circumvent the problem of passing density as an input parameter to the routine, we interface the original `helmeos` with a zero-finding routine that calls it repeatedly with different values of ρ until convergence in pressure is achieved. Subsequent calls use the previous value of ρ as an initial guess. Given the Courant conditions we impose, the information in each grid point does not change much in one time step, and convergence is achieved within two or three calls. This is done in parallel for each grid point.

The choice for the EOS is important for the evolution equation for the temperature T . We still derive it from the first law of

thermodynamics:

$$\frac{DE}{Dt} = \frac{1}{\rho^2} P \frac{D\rho}{Dt} + Q \quad (9)$$

(where E and Q are the energy and heating rate per unit mass), but we have two different results depending on the choice of the EOS. If we use the perfect gas EOS, the evolution equation for temperature has the form (compare to BC, eq. 20):

$$\frac{c_P}{\mu} \frac{DT}{Dt} = \frac{1}{\rho} \frac{DP}{Dt} + \frac{c_P T}{12} \left(17 \frac{DX}{Dt} + 2 \frac{DY}{Dt} \right) + Q, \quad (10)$$

where $c_P = R(\gamma - 1)/\gamma$, γ is the adiabatic index and $R = 8.3144621 \times 10^7 \text{ erg K}^{-1} \text{ mol}^{-1}$ is the gas constant³.

When we include electron degeneracy and radiation pressure, by contrast, we have

$$\tilde{c}_P \frac{DT}{Dt} = A \frac{DP}{Dt} + B \frac{DX}{Dt} + C \frac{DY}{Dt} + Q, \quad (11)$$

with

$$D = \left(\frac{P}{\rho^2} - \frac{\partial E}{\partial \rho}_{T,X,Y} \right) \quad (12)$$

$$A = D \frac{\partial \rho}{\partial P}_{T,X,Y} \quad (13)$$

$$\tilde{c}_P = \left(\frac{\partial E}{\partial T}_{\rho,X,Y} - D \frac{\partial \rho}{\partial T}_{P,X,Y} \right) \quad (14)$$

$$B = - \left(\frac{\partial E}{\partial X}_{\rho,T,Y} - D \frac{\partial \rho}{\partial X}_{P,T,Y} \right) \quad (15)$$

$$C = - \left(\frac{\partial E}{\partial Y}_{\rho,T,X} - D \frac{\partial \rho}{\partial Y}_{P,T,X} \right), \quad (16)$$

where we make use of the relations

$$\frac{\partial \rho}{\partial P}_{T,X,Y} = \frac{1}{\partial P / \partial \rho}_{T,X,Y} \quad (17)$$

$$\frac{\partial \rho}{\partial T}_{P,X,Y} = - \frac{\partial P / \partial T}_{\rho,X,Y}}{\partial P / \partial \rho}_{T,X,Y} \quad (18)$$

$$\frac{\partial \rho}{\partial X}_{P,T,Y} = - \frac{\partial P / \partial X}_{\rho,T,Y}}{\partial P / \partial \rho}_{T,X,Y} \quad (19)$$

$$\frac{\partial \rho}{\partial Y}_{P,T,X} = - \frac{\partial P / \partial Y}_{\rho,T,X}}{\partial P / \partial \rho}_{T,X,Y}, \quad (20)$$

since the routine returns variables as functions of ρ , T , X and Y .

A further complication comes from the fact that `helmeos` actually uses $\bar{A} = 12/(1 + 11X + 2Y)$ and $\bar{Z} = \bar{A}(1 + X)/2$, (instead of X and Y directly) for P , and that the derivatives of E and P are evaluated with respect to T , \bar{A} , \bar{Z} and ρ . Therefore, for equations (15), (16), (19) and (20) we also need

$$\frac{\partial}{\partial X} = - \frac{\bar{A}^2}{12} \left(11 \frac{\partial}{\partial \bar{A}} + (5 - Y) \frac{\partial}{\partial \bar{Z}} \right) \quad (21)$$

$$\frac{\partial}{\partial Y} = - \frac{\bar{A}^2}{12} \left(2 \frac{\partial}{\partial \bar{A}} + (1 + X) \frac{\partial}{\partial \bar{Z}} \right) \quad (22)$$

The final evolution equation for the temperature is therefore ($D/Dt = \partial/\partial t + \mathbf{u} \cdot \nabla_\sigma + \dot{\sigma} \partial/\partial \sigma$):

$$\partial T / \partial t = T_{t,\text{adv}} + T_{t,\text{thermodyn}} + Q / \tilde{c}_P, \quad (23)$$

² Available at http://cococubed.asu.edu/code_pages/eos.shtml.

³ Note that in BC we included μ in the definition of R .

where the contributions to $\partial T/\partial t$ are separated into

$$T_{t,\text{adv}} = -(\mathbf{u} \cdot \nabla_{\sigma} T + \dot{\sigma} \partial T/\partial \sigma) \quad (24)$$

$$T_{t,\text{thermodyn}} = \frac{A}{\tilde{c}_P} \frac{DP}{Dt} + T_{t,\mu} \quad (25)$$

$$T_{t,\mu} = \frac{B}{\tilde{c}_P} \frac{DX}{Dt} + \frac{C}{\tilde{c}_P} \frac{DY}{Dt} \quad (26)$$

and Q/\tilde{c}_P , so that we can test the relative importance of the contributions of the different terms (see Sec. 3.4). Q is further divided into $Q = Q_n + Q_{\text{cond}} + Q_{\text{cool}} + Q_{\text{hyper}}$, where Q_n is the nuclear burning contribution, Q_{cond} is the conduction contribution and Q_{cool} is the cooling contribution from the top (see the next sections). We also include an artificial diffusive term Q_{hyper} (with a small coefficient, see Sec. 3.4 of BC) to ensure numerical stability. In the case of the perfect gas EOS the evolution equation is very similar to equation (23).

Finally, the term DP/Dt is evaluated according to equation (19) of BC, which does not depend on the EOS, but on the choice of the σ -coordinate system. DX/Dt and DY/Dt have to be treated carefully: in the case of reactions, or any change in composition, they have to be evaluated explicitly (see Sec. 2.3).

2.2 Conduction

Since conduction may play an important role in flame propagation, we include a physical conduction term in Q of the form:

$$Q_{\text{cond}} = \frac{1}{\rho} \nabla \cdot \left(\frac{16\sigma_B T^3}{3\rho\kappa_c} \nabla T \right) \quad (27)$$

where κ_c is the effective opacity due to both radiative and conductive processes. In the σ -coordinate system Q_{cond} takes the form:

$$\begin{aligned} \frac{1}{P_*} \left\{ \nabla_{\sigma} \left[\frac{16\sigma_B T^3}{3\kappa_c \rho} \left(\frac{P_*}{\rho} \nabla_{\sigma} T + \nabla_{\sigma} \phi \frac{\partial T}{\partial \sigma} \right) \right] + \right. \\ \left. + \frac{\partial}{\partial \sigma} \left[\frac{16\sigma_B T^3}{3\kappa_c P_*} \left(\nabla_{\sigma} \phi^2 \frac{\partial T}{\partial \sigma} + \frac{P_*}{\rho} \nabla_{\sigma} \phi \nabla_{\sigma} T + \right. \right. \right. \\ \left. \left. \left. + g^2 \frac{\partial T}{\partial \sigma} \right) \right] \right\} \quad (28) \end{aligned}$$

where $\phi = gz = P_* \int_{\sigma}^1 1/\rho d\sigma'$. The terms that include ϕ are due to the fact that the transformation matrix between the Cartesian coordinate system and the σ coordinate system is not everywhere orthogonal. These contributions turn out to be small and can be neglected.

We have implemented two possibilities for evaluating κ_c : either it has a fixed value set at the beginning of the simulation, or it is calculated for each and every grid point taking into account the composition and thermodynamical variables at that position. For this second option we adapted the publicly available routines of Timmes: `sig99`⁴. The opacities calculated in this way take into account radiation, scattering and the degree of degeneracy (see Timmes 2000, and references therein). Based on the values of density, temperature and composition in the simulations that we wanted to perform, we decided to use an average constant value of $\kappa_c = 0.07 \text{ cm}^2 \text{ g}^{-1}$ in our reference simulation, which speeds up the calculations whilst still preserving the critical physics.

As anticipated in section 2.1, we include in equation (23) a hyperdiffusive term (see BC, section 3.4.2), which mimics conduction. This term is unphysical and only used to ensure numerical

stability. In the horizontal direction, in particular, it will be unphysically high, and may partly limit the conclusions we can draw from our simulations. However, test runs involving much lower hyperdiffusivity yielded flame velocities (see section 3.2) which differ by only a few percent from the values reported in this paper.

2.3 Sources and sinks of heat: nuclear burning and cooling

Since we are interested in simulating Type I bursts, we implement helium burning via the triple- α reaction according to (see Clayton 1984):

$$Q_n = 5.3 \times 10^{18} \rho_5^2 \left(\frac{Y}{T_9} \right)^3 e^{-4.4/T_9} \text{ erg g}^{-1} \text{ s}^{-1}, \quad (29)$$

where T_9 is the temperature in units of 10^9 K , Y is the mass fraction of He and ρ_5 is the density in units of 10^5 g cm^{-3} . Including only the triple- α process is of course a simplification, since there are many other reaction chains that should be taken into account (this model would not be correct even for a pure He accretor). However we leave this refinement for later investigation.

During burning the composition is evolved according to

$$\frac{DY}{Dt} = -\frac{Q_n}{\epsilon_{\alpha}} \quad (30)$$

which corresponds to

$$\frac{\partial Y}{\partial t} = -\mathbf{u} \cdot \nabla_{\sigma} Y - \dot{\sigma} \frac{\partial Y}{\partial \sigma} - \frac{Q_n}{\epsilon_{\alpha}} \quad (31)$$

where the first two terms come from advection and the third is the consumption of He due to nuclear reactions ($\epsilon_{\alpha} = 5.84 \times 10^{17} \text{ erg g}^{-1}$ is the energy production per gram per nucleon). We also include a form of artificial diffusion as described in Sec. 3.4 of BC to ensure numerical stability.

In terms of sinks of entropy, we include the possibility of cooling from the uppermost layers. We use a simple formula, derived under the assumption that energy is only transported through the layers above the simulated computational domain, without additional sinks or sources within the atmosphere. This is a somewhat coarse approximation, particularly since expansion of the upper layers may occur. We use the temperature of the top grid cell in order to evaluate the flux due to radiation and conduction:

$$F = \frac{16\sigma_B}{3\rho\kappa_c} T^3 \frac{dT}{dz} \quad (32)$$

where F is the flux, which we assume to be constant in our plane parallel approximation and σ_B and κ_c are as defined in Sec. 2.2. We further assume that κ_c is constant in the layers above the simulation. Rearranging and integrating in the vertical, z , direction, from the top of the simulation (T) to the top of the NS atmosphere (atm), we have

$$F \int_{\text{atm}}^{\text{T}} \rho dz = \frac{16\sigma_B}{3\kappa_c} \int_{\text{atm}}^{\text{T}} T^3 dT. \quad (33)$$

In hydrostatic equilibrium, the integral on the left hand side reduces to P_{T}/g , so that

$$F \frac{P_{\text{T}}}{g} = \frac{4\sigma_B}{3\kappa_c} T^4 \Big|_{\text{atm}}^{\text{T}} \quad (34)$$

Then, assuming that the temperature at the top of the atmosphere is negligible with respect to that at the top of the simulation, we obtain

$$F = \frac{4\sigma_B}{3\kappa_c P_{\text{T}}/g} T_{\text{T}}^4 \quad (35)$$

⁴ Available at http://cococubed.asu.edu/code_pages/kap.shtml.

This is the flux from the surface of a grid cell at the top of the simulation. In order to derive the entropy loss per unit mass, we multiply the flux by the surface area S of the cell and divide by the mass within it:

$$Q_{\text{cool}} = F \frac{S}{\rho_{\text{T}} S \Delta z_{\text{T}}} \quad (36)$$

so that ($\Delta z \sim H \sim P_{\text{T}}/g\rho_{\text{T}}$)

$$Q_{\text{cool}} = \frac{4g^2 \sigma_{\text{B}} T_{\text{T}}^4}{3\kappa_{\text{c}} P_{\text{T}}^2} \quad (37)$$

This is the sink term we use in our simulations; it could also be used as a first approximation to calculate the bolometric lightcurve of the bursts.

2.4 Tracer particles

Finally, we add the capability to follow tracer particles. These are assigned initial positions uniformly distributed in the integration domain and are evolved according to

$$\frac{dx}{dt} = u_x(x, y, \sigma) \quad (38)$$

$$\frac{dy}{dt} = u_y(x, y, \sigma) \quad (39)$$

$$\frac{d\sigma}{dt} = \dot{\sigma}(x, y, \sigma) \quad (40)$$

where d/dt is the rate of change of the particle's position in σ coordinates. Time evolution is the same as for all of the other variables (see BC, section 3.3), and the values of the three components of the velocity at arbitrary points within each grid cell are derived by means of bilinear interpolation (Press et al. 1992) of the fluid velocity⁵.

3 FLAME PROPAGATION SIMULATIONS

In this section we describe the numerical setup used for all the simulations and then provide a description of what we see in the runs. Finally, we describe our interpretation of what drives the flame propagation.

3.1 Numerical setup

We ran a series of simulations resolving both the horizontal x and vertical z directions, assuming that the dynamical variables are independent of the y coordinate (making the simulations effectively 2D). The fixed initial conditions, common to all of our simulations, are

$$\begin{aligned} P_{\text{T}} &= 10^{22} \text{ erg cm}^{-3} & P_* &= (e^{1.7} - 1) \times 10^{22} \text{ erg cm}^{-3} \\ X &= 0 & Y &= 1 \\ \nu_1 &= 0.03 & \nu_2 &= 0.5 \end{aligned}$$

and

$$T_0 = 10^8 \text{ K} \quad \delta T = 3.81 \times 10^8 \text{ K}$$

⁵ We also tested higher order interpolation methods, but found no significant differences.

where P_{T} and P_* are the pressure at the top and the difference between the bottom and top pressure (see BC, section 2). Note that whilst P_{T} is constant, P_* is a function of horizontal position and time, but not of σ . The choice of P_* means that we simulate 1.7 scale heights. ν_1 and ν_2 are the kinetic diffusive coefficients (see section 3.4 of BC). The corresponding coefficients for the temperature and the composition fractions X and Y are taken to be 1% of these values.

We also use a common initial temperature perturbation in all simulations. We use a z -independent temperature profile, which varies in the horizontal direction according to:

$$T = T_0 + \frac{\delta T}{1 + \exp[(x - 1.2 \text{ km})/0.36 \text{ km}]} \quad (41)$$

This function ensures that the temperature profile is smooth enough that it does not cause numerical issues; 1.2 km corresponds to the position where the temperature perturbation of the background T_0 is half of its maximum, while 0.36 km is approximately half the width between where the perturbation is asymptotic to its maximum and where it is asymptotic to its minimum (0 K).

We simulate a domain with a horizontal extent of 7.5 km, which allows more than sufficient room for the propagating flame to reach a steady state. The initial conditions have a high temperature at one end of the domain, so the flame ignites there and propagates towards the other end. In some sense the point where ignition occurs can be thought of as the eye of the cyclonic system⁶. We use symmetric boundary conditions in the vertical direction and reflective conditions in the horizontal direction. In all simulations presented here, we use horizontal and vertical resolutions of 240 and 90. Gravitational acceleration $g = 2 \times 10^{14} \text{ cm s}^{-2}$ and we use the plane-parallel approximation and a constant Coriolis parameter ($f = 2\Omega$), i.e. the f -plane approximation. The fluid is at rest at the beginning, $U_x = 0 \text{ cm s}^{-1}$, and quickly adjusts to the Rossby solution (see BC, sec. 4.2) before the flame spreads.

Since we want to study the effects of different rotation frequencies and the influence of conduction, we run a series of models employing different values of the spin frequency Ω and the opacity κ_{c} . The parameters for the simulations that we run are given in Table 1.

To help us find out how the flame propagates, we use test particles and follow what happens to these fluid elements before, during, and after ignition conditions are met. We place the test particles homogeneously in our grid (note that they are not homogeneous in space since we use a pressure coordinate system) such that $x_{i,j} = i * \delta x / 200$ and $\sigma_{i,j} = j * 1/200$, $i, j \in [1, 200]$. We also track what happens at three different points in the atmosphere with fixed horizontal position. These points rise and descend with time, having fixed values of σ not z , so this approach is not strictly speaking Eulerian. However it still allows us to see what happens when the flame reaches a determined distance from the ignition point.

3.2 General description of the propagating flame

In this section, we give a qualitative description of the burning fluid as a whole. We begin by using one particular run as an example, since the qualitative behaviour is general. The left hand column of Fig. 1 shows the fluid in its initial conditions for reference

⁶ A cyclone is a system of circulating fluid where, at a given height, the pressure at the centre is lower than at the sides. The fluid is drawn in at the bottom and launched to the top from the centre.

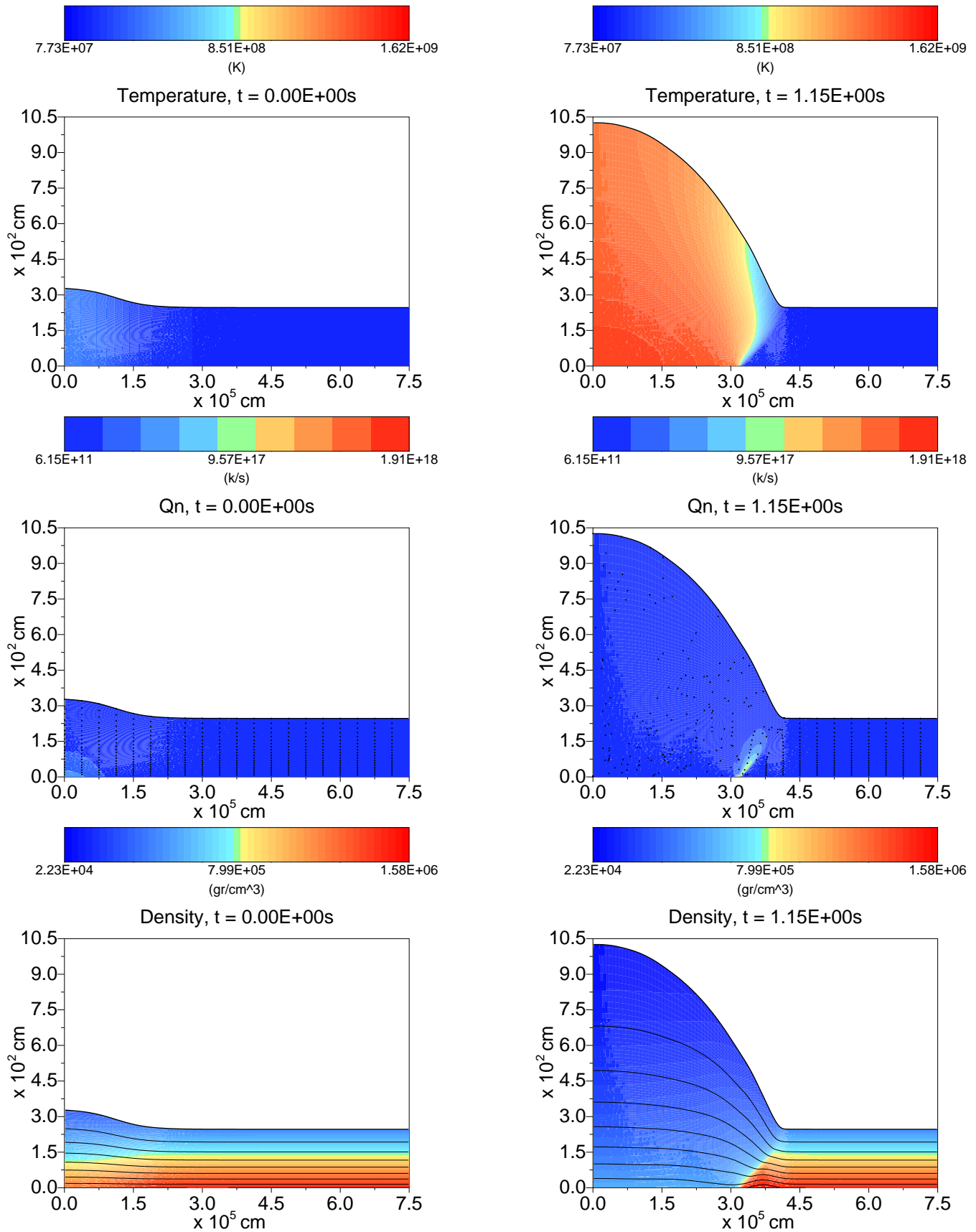


Figure 1. Initial conditions (left) and conditions at $t = 1.15 \text{ s}$ (right), when the flame is steadily propagating, for reference simulation 6. The top panels show the temperature, the middle ones show burning rate with the tracer particles superimposed and the bottom panels show density with isobars superimposed (10 levels from $P = 10^{22}$ to $6.2 \times 10^{22} \text{ erg cm}^{-3}$). Note the different horizontal and vertical scales.

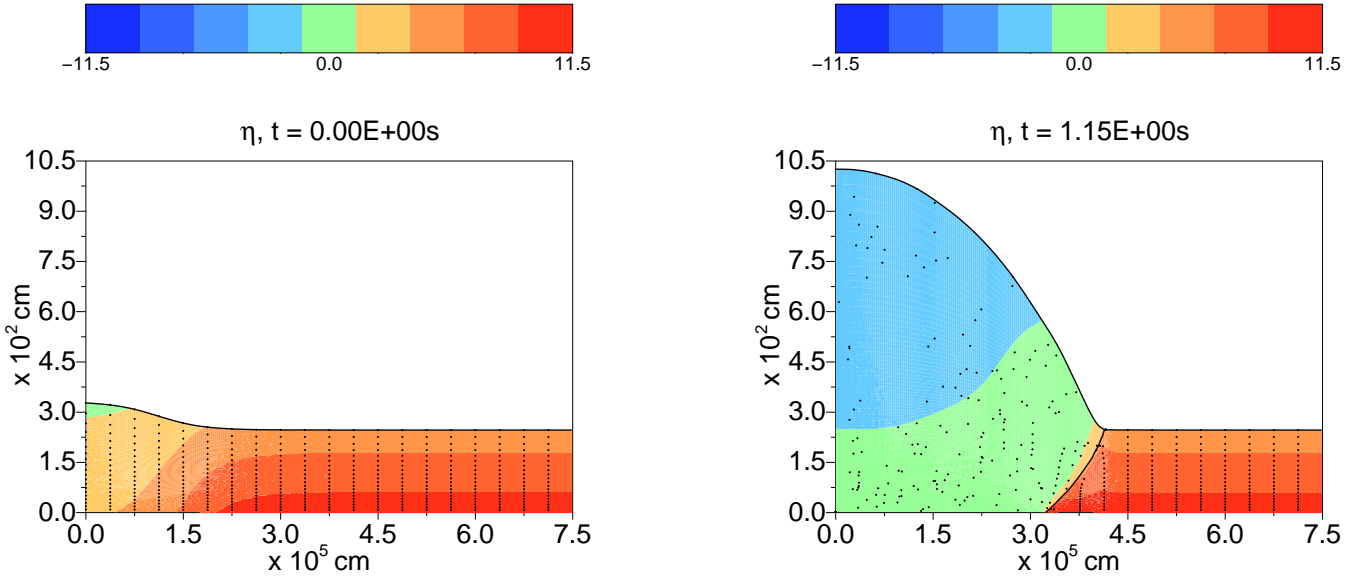


Figure 2. Electron chemical potential η at the beginning and at $t = 1.15$ s for reference run 6. Degeneracy decreases with lower η . The electrons are always partially degenerate, but degeneracy is partially lifted when the flame passes through. The black line again indicates the position of the interface.

Run	ν (Hz)	κ_c (g cm $^{-2}$)	v_f (cm s $^{-1}$)
1	450	$1 \times 10^{+0}$	$(1.33 \pm 0.03) \times 10^5$
2	450	7×10^{-1}	$(1.43 \pm 0.02) \times 10^5$
3	450	5×10^{-1}	$(1.52 \pm 0.02) \times 10^5$
4	450	3×10^{-1}	$(1.67 \pm 0.03) \times 10^5$
5	450	1×10^{-1}	$(1.91 \pm 0.04) \times 10^5$
6	450	7×10^{-2}	$(2.01 \pm 0.05) \times 10^5$
7	450	5×10^{-2}	$(2.03 \pm 0.05) \times 10^5$
8	450	1×10^{-2}	$(1.99 \pm 0.02) \times 10^5$
9	450	1×10^{-3}	$(1.98 \pm 0.03) \times 10^5$
10	50	7×10^{-2}	$(1.11 \pm 0.18) \times 10^6$
11	112.5	7×10^{-2}	$(5.30 \pm 0.31) \times 10^5$
12	225	7×10^{-2}	$(3.04 \pm 0.10) \times 10^5$
13	900	7×10^{-2}	$(1.39 \pm 0.02) \times 10^5$

Table 1. Values of the spin frequency $\nu = \Omega/2\pi$ and the opacity κ_c used in the different simulations. In the third column we report the velocity of the flame as measured from the simulations, with errors derived from the least squares fit (see section 3.2). See Appendix A for a discussion about the convergence rate of the code and values of the flame speed.

run 6. The right hand column shows the conditions at $t = 1.15$ s, when the flame is propagating steadily. The upper panels show the temperature distribution, and the middle ones the burning rate. In these panels we superimpose our tracer particles. The bottom panels show the density, with the iso-surfaces of pressure (isobars) superimposed.

In the top left panel of Fig. 1 the fluid is hotter on the left of the image: this is the initial perturbation, where the temperature is $T = 4.81 \times 10^8$ K, while at the other side the temperature is $T = 10^8$ K. Moving to the right-hand panel, we see that the flame front has moved to the right. Where the fluid has already burnt, it is hotter ($T \sim 10^9$ K) and has expanded by a factor of the order of 4.⁷ Looking at the middle panels we can see that the tracer particles

have been scattered by the passage of the front, while the lower panels show a drop in density. Eventually, after the flame has passed (not shown in the figure), the burning diminishes, the temperature decreases and the fluid contracts.

Looking more closely at the propagating front, we see that it is characterized by a slanted interface between the hot burning fluid on the left, and the cold unburnt fluid on the right (in Fig. 1 right, the interface lies roughly between $x = 3.7 \times 10^5$ and 4.7×10^5 cm). We see a decrease in pressure on the left of the interface and an increase immediately to the right of it (see the lowest isobars in the bottom right panel of Fig. 1). They reflect a change in P_* (equation 1). Because of the hydrostatic approximation, P_* is a measure of the column density at each point. A change in P_* means horizontal mass motion. The decrease before the front and the increase after it therefore show that there has been a motion of matter from behind the front forward.

The electrons are partially degenerate, as can be seen from Fig. 2 where we plot the electron chemical potential. The electrons remain partially degenerate throughout all the simulations, but the degeneracy is lifted by the flame (as can be seen also by the fact that the temperature increases by a factor ~ 15 , while the height of layer increases by only a factor of 4 or 5) so that in the hot fluid the perfect gas pressure and the radiation pressure become more important.

The peak of the burning is concentrated in a thin stripe along the interface (Fig. 1, middle right panel) where the density is still high (undiminished by the increase in temperature) and the fuel is still almost pure Helium. We also observe tracer particles moving in the vertical plane, primarily along the interface and in the region to the left of it.

In order to understand what is driving the flame forward, we measure the different terms in the energy equation (23): conduction $Q_{\text{cond}}/\dot{c}_P$, advection $T_{\text{t,adv}}$ (motion of the fluid) and thermodynamic compression $T_{\text{t,thermodyn}}$. For each term, we plot the contributions in Fig. 3. In the four panels the black line approximates the interface between hot and cold fluid. It is drawn below the region of significant burning in order to clearly demarcate re-

⁷ In general, the maximum expansion factor can be up to $\sim 4 - 5$ depending on the effective opacity κ_c that sets the cooling rate.

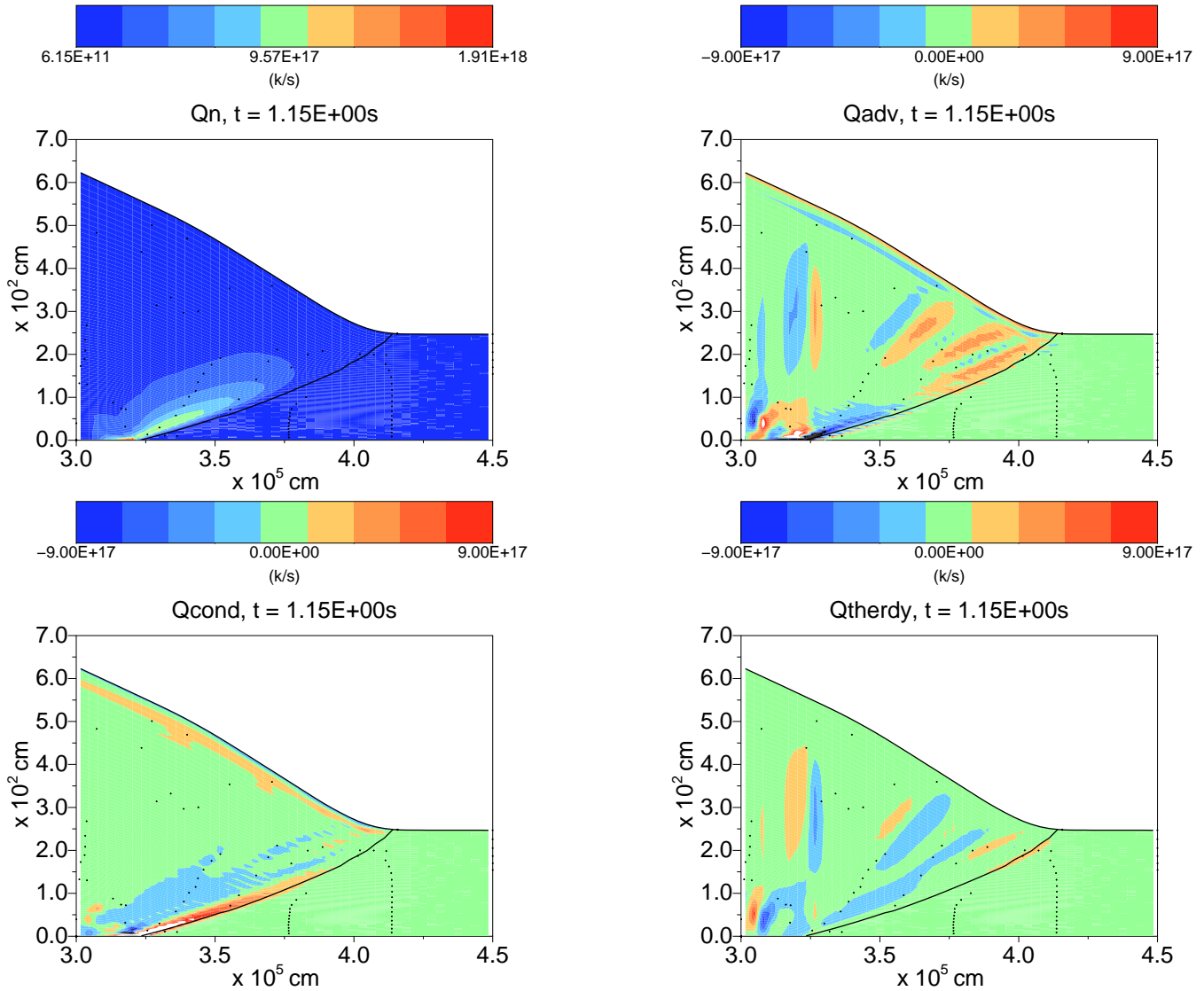


Figure 3. Burning rate and heating rate associated with advection $T_{t,adv}$, conduction Q_{cond}/\tilde{c}_P and thermodynamical compression $T_{t,thermodyn}$ for reference simulation 6. The black line indicates the hot-cold fluid interface. The colour scale has been restricted to highlight details (the white regions indicate values above the maximum of the scale and the black ones values below the minimum).

regions where burning has started from those where burning is about to start.

It is clear from Fig. 3 that in the region immediately below the peak of the burning, heat conduction is much more important in increasing the temperature in the unburnt fuel region than both the effects of mixing (measured by the advection of temperature) or thermodynamic compression. It is this process that drives flame propagation, since the main burning occurs in this zone. In the upper part of the interface, advection and thermodynamic compression dominate heat transfer to the unburnt region. That picture is confirmed by observing what happens at a fixed horizontal position. In Fig. 4 we plot the burning rate versus temperature and density, and temperature and density versus time for three different positions: at the top, in the middle and at the bottom of the fluid at a fixed horizontal position $x = 3.3 \times 10^5$ cm. It can be seen that the topmost point (black) in the figure is compressed and its temperature rises. The lower points then follow, but the burning does not really start until the temperature has risen sufficiently. The

same figure also demonstrates how the burning rate increases with increasing temperature, while the correlation with density (see for example the lower panel) is not as strong. The decrease of burning rate at the end of the curves is due to the consumption of fuel which eventually becomes the most important factor.

Directly above the flame, on the other hand, heat conduction is not effective, while the advective and thermodynamic compressive terms show opposite signs. This is a clear signature of convection, which is expected above the burning regions. We note that the convective cells near the topmost part of the hot-cold interface are mostly parallel to it (i.e. almost horizontal, recall the extreme aspect ratio of the interface), while the ones behind the interface are vertical⁸. In Fig. 5 we plot contours of the total entropy per unit mass as returned by the code `helmeos`.

To compute flame propagation speed from our simulations, we

⁸ We want to stress that also these vertical cells are actually elongated in the horizontal direction due to the aspect ratio of our underlying grid cells.

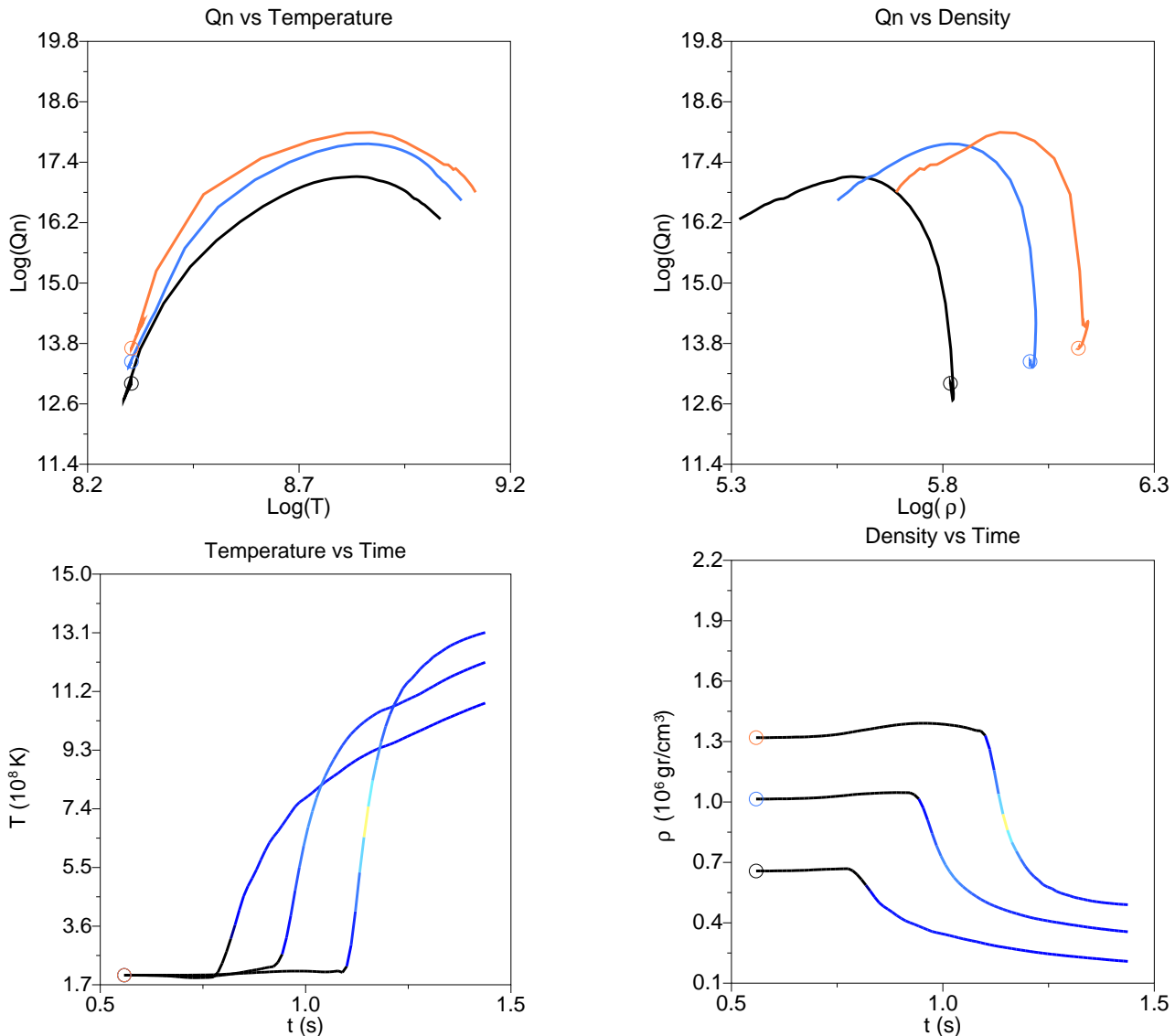


Figure 4. Top: burning rate versus temperature and density for three different points fixed relative to the grid, i.e. at fixed $x = 3.3 \times 10^5$ cm and sigma: near the top (black), in the middle (blue) and near the bottom (orange). Bottom: temperature and density versus time for the same points. The lines in the lower panels have colours corresponding to the same scale as the contours for the burning rate in the middle panel of Fig. 1. The circles indicate the origin of the curves. The strong relation between their burning rate and temperature is clear, while the importance of the change of density appears to be less.

define the front position as the location with the maximum burning rate. In Fig. 6, we follow the position of the front for simulation 6 and plot it versus time. At the beginning there is a transitional stage after the flame is started by the initial perturbation of the temperature and the front adjusts to a steadily spreading configuration (in $\lesssim 0.1$ s). This steady propagation is well fitted by a straight line, and the gradient gives us the speed of the flame front. We repeat the fit procedure for all of the various runs: the resulting front speeds v_f are reported in Table 1.

Having measured front velocities, we can determine the effects of the rotational spin Ω and the effective opacity κ_c (a proxy for the heat conductivity). Overall, the gradient of the lifted fluid is steeper for higher Ω , and the baroclinicity (the misalignment between the iso-surfaces of density and pressure measured by $\nabla P \times \nabla \rho$) along the interface tends to increase with Ω . The flame propagation speed decreases as the rotation rate increases (see the next sections and Fig. 9). Changing κ_c also has an effect on flame

velocity: the flame is faster for lower κ_c , but the velocity saturates when $\kappa_c \lesssim 10^{-2}$ cm 2 g $^{-1}$ (see Fig. 10).

In Appendix A we discuss the convergence rate of the code. Even though the rate is lower than desirable, so that the actual values of the flame speed should be slightly different in reality, we can be confident that the general conclusions we draw are solid. In particular, increasing the resolution decreases the flame speed, which is indicative of the fact that a detonation would not develop. Moreover, the flame always reaches a steady state and the structure of the front is as described above and in the following.

3.3 A first set of conclusions

Although the fluid moves ageostrophically from behind the interface forward, this motion does not go past the interface (Fig. 1 bottom right). We interpret this as follows: the fluid has expanded on the left of the front because of its higher temperature, and the re-

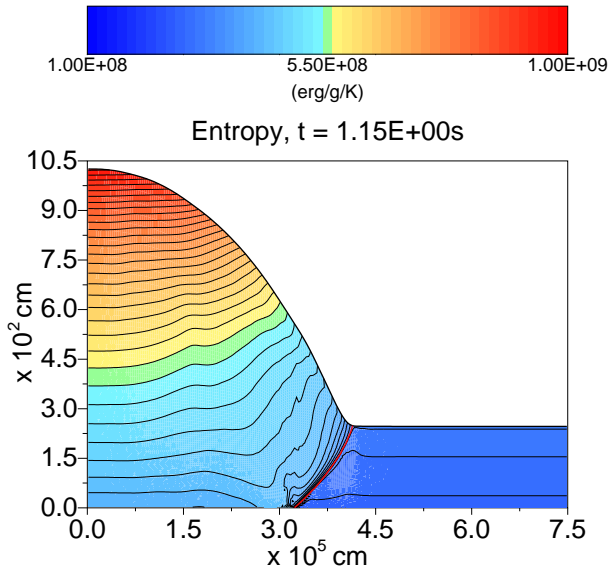


Figure 5. Entropy per unit mass (radiation, ion and electron gas) for reference simulation 6 at $t = 1.15$ s. The black lines indicate the contours for better visualization. The red line indicates the position of the interface.

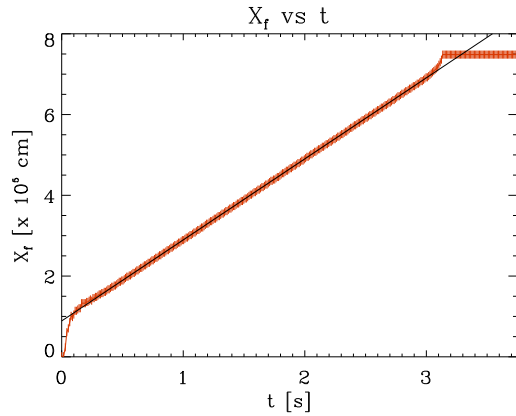


Figure 6. Flame front position for run 6. The symbols indicate the error bars on the positions, while the line shows the best linear least squares fit. After an initial stage, the flame adjusts to steady propagation. Eventually, the flame reaches the opposite boundary (in this case in ~ 3 s).

sulting horizontal pressure gradient pushes the hot burning fluid to spill over the unburnt fluid. The Coriolis force, however, diverts the horizontal x motion into the horizontal y direction and thus creates a geostrophic current that compensates for the horizontal pressure gradient. The resulting configuration is that of the Rossby adjustment problem (see BC), as anticipated by SLU. In this case the inclination angle α of the interface should be $\alpha \sim H/R_{\text{Ro}}$, where H is the scale height of the fluid and R_{Ro} is the Rossby radius $R_{\text{Ro}} = \sqrt{gH}/2\Omega$ (where $\Omega = 2\pi\nu$ and ν is the spin frequency of the NS). Measuring the slope of the black line in Fig. 3, we find that the slope is $\alpha \sim 3.5 \times 10^{-3}$, so that its horizontal extent is $\sim 2 - 3R_{\text{Ro}}$. This is in accordance with expectations.

Regarding the motion that we observe in the vertical plane along the interface, we note that here the fluid is much more baroclinic, that is to say, the iso-surfaces of density and pressure are much more misaligned than elsewhere, as can be seen in the lower

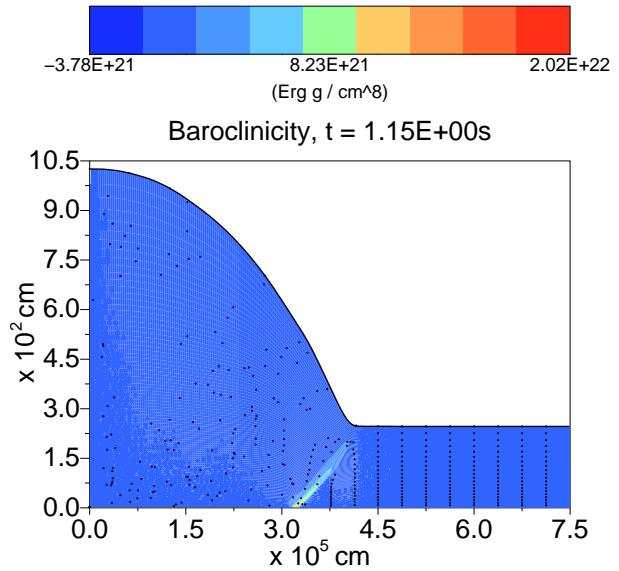


Figure 7. Baroclinicity: $\nabla P \times \nabla \rho$, for reference simulation 6. The vector is along the y direction, coming out of the plane.

right panel of Fig. 1 and in Fig. 7. It is well known from geophysical studies that geostrophic balance is unstable in the presence of baroclinicity. The resulting instability is similar in nature to convection, but with motion, which is no longer vertical, lying within the “wedge of instability” between the iso-surfaces of pressure and density (Pedlosky 1987). Fujimoto (1988, 1993) and Cumming & Bildsten (2000) in fact already studied the possibility of baroclinic instability in the context of Type I bursts, but their baroclinicity was very mild since they considered the effects of shear induced by the differential rotation due to the vertical expansion of the burning layer, and not the effects of the huge horizontal temperature gradients that develop during flame propagation.

In our case, the source of baroclinicity is the horizontally-inhomogeneous nuclear burning⁹ which affects the temperature profile. Its steady propagation is maintained by the Coriolis force, which reinforces the near-geostrophic configuration on time scales of the order of $1/\nu$. Following the tracer particle motion, we can see advection along and in front of the interface, which we attribute to the development of baroclinic instability. In the previous section we noted the presence of cells that are highly elongated in the horizontal direction at the upper end of the hot-cold fluid interface: we identify these cells with baroclinicity-induced motion. Fig. 8 shows how particles are driven into the front and down along the interface. After the flame has passed and the front is farther away, the particles are caught by the advective motion and driven upwards. The ascending part is different for different particles and this picture just indicates the general trend.

3.4 Front propagation mechanism

Summarizing the results from section 3.2, we see that at the top of the interface the fluid is heated up by the spilling over of the hot fluid, via advection and thermodynamics. However, in the most relevant regions for flame propagation, heat is brought across the interface primarily by conduction (mainly vertically given the small

⁹ Compare Fig. 7 to the middle right panel of Fig. 1.

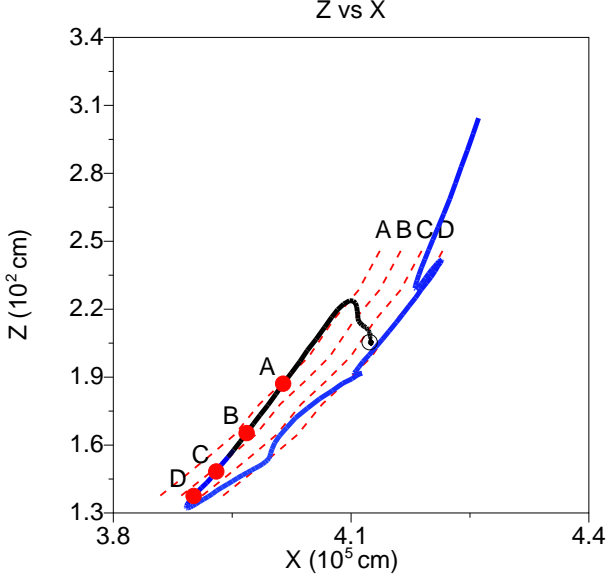


Figure 8. Example of motion of one tracer particle on the vertical plane. The red dashed lines indicate the position of the flame front at different times A, B, C and D. The corresponding positions of the particle are indicated by the same letters on the particle trajectory. The empty circle indicates the starting point. The colours of the trajectory correspond to the same scale as the contours for the burning rate in the middle panel of Fig. 1.

inclination angle¹⁰), with a contribution from baroclinic instability mixing.

The contribution to $\partial T/\partial t$ in equation (23) from conduction can be written by means of equation (27) as

$$T_{t,\text{cond}} = \frac{Q_{\text{cond}}}{\tilde{c}_P} = \frac{1}{\tilde{c}_P \rho} \nabla \cdot \left(\frac{16 \sigma_B T^3}{3 \rho \kappa_c} \nabla T \right). \quad (42)$$

From this we can derive an approximate diffusion coefficient for conduction D_{cond} as

$$D_{\text{cond}} \sim \frac{16 \sigma_B T^3}{3 \tilde{c}_P \rho^2 \kappa_c} \quad (43)$$

and then derive the timescale for heat diffusion across the vertical scale height H as $\tau_{\text{cond}} \sim H^2/D_{\text{cond}}$, or

$$\tau_{\text{cond}} \sim \frac{3}{16} \frac{\rho^2 H^2 \tilde{c}_P \kappa_c}{\sigma_B T^3} \quad (44)$$

Equation (44) gives

$$\tau_{\text{cond}} \sim 2.1 \times 10^{-2} \text{ s} \left(\frac{\kappa_c}{0.07 \text{ cm}^2 \text{ g}^{-1}} \right) \left(\frac{\rho}{10^5 \text{ g cm}^{-3}} \right)^2 \left(\frac{T}{10^9 \text{ K}} \right)^{-3} \left(\frac{H}{3 \times 10^2 \text{ cm}} \right)^2 \left(\frac{\tilde{c}_P}{10^8 \text{ erg K}^{-1}} \right) \quad (45)$$

Once the lower fluid has been heated up and starts burning it expands again. The Coriolis force then reinforces Rossby adjustment in a time scale of the order of $\nu^{-1} \ll \tau_{\text{cond}}$. This translates a small vertical shift into a long horizontal displacement, where the proportionality is given by the inclination of the interface: $1/\alpha \sim (2 - 3R_{\text{Ro}})/H$, as we will see in the next section.

¹⁰ Heat conduction in the horizontal direction can be neglected since the horizontal length scale is larger by a factor $\sim 10^3$ than the vertical length scale. Two runs where in one case full conduction was implemented and in the other only vertical conduction was used gave virtually identical results.

Run	$D_{\perp\text{bar}}$	τ_{bar}	τ_{cond}	$\tau_{\text{bar}}/\tau_{\text{cond}}$
1	223.0	403.6	142.5	2.8
2	288.6	311.8	99.8	3.1
3	328.9	273.6	71.3	3.8
4	449.5	200.2	42.8	4.7
5	915.0	98.4	14.3	6.9
6	926.0	97.2	10.0	9.7
7	1045.1	86.1	7.1	12.1
8	2047.2	44.0	1.4	31.4
9	7757.8	11.6	0.1	116.0
10 ^a	—	—	10.0	—
11 ^a	—	—	10.0	—
12	548.4	164.1	10.0	16.4
13	1570.9	57.3	10.0	5.7

Table 2. Diffusion coefficient for the baroclinicity driven advection (equation 47) as measured directly from the simulations, its diffusion timescale according to equation (46) and the timescale for conduction as from equation (45), using $T = 6 \times 10^8$ K and $\rho = 9 \times 10^5$ g cm⁻³. The last column reports the ratio between the two timescales. Note that these values are only indicative order of magnitude estimates.

^a These runs had less clear configurations, so that reliable measurements were not possible.

The effective advective conduction brought about by baroclinic mixing would act on a time scale given by

$$\tau_{\text{bar}} \sim H^2/D_{\perp\text{bar}}, \quad (46)$$

with

$$D_{\perp\text{bar}} \sim w_{\perp\text{bar}} \lambda_{\perp\text{bar}}, \quad (47)$$

where $w_{\perp\text{bar}}$ and $\lambda_{\perp\text{bar}}$ are the physical velocity of the fluid and its length scale perpendicular to the hot-cold fluid interface.

As long as $\tau_{\text{bar}} \gg \tau_{\text{cond}}$, conduction will be the most effective mechanism. In order to get a handle on the importance of the baroclinicity induced advection, we measured the average values of $w_{\perp\text{bar}}$ and $\lambda_{\perp\text{bar}}$. For each grid point along the interface, we calculated the component of fluid velocity in the direction perpendicular to the interface. Considering only the region over which $w_{\perp\text{bar}}$ was negative, we calculated the average $w_{\perp\text{bar}}$ and measured $\lambda_{\perp\text{bar}}$ as the length of this region in the direction perpendicular to the interface. We then calculated the total average $D_{\perp\text{bar}}$: the results are reported in Table 2 for all of the simulations. The results confirm that baroclinicity is negligible most of the time, apart from in the cases of very low heat diffusivity (high κ_c). One should be aware, however, that all these values are order of magnitude estimates, and hence only describe trends, not precise timescales.

3.5 Front propagation speed

Following e.g. Landau & Lifshitz (1959) and Fryxell & Woosley (1982b), the velocity of flame propagation across the interface should be given, in a deflagration regime, by

$$v_{f\perp} \sim \sqrt{\frac{D_{\text{cond}}}{\tau_n}} \quad (48)$$

where τ_n is the burning time scale, given by $\tau_n = \epsilon_\alpha/Q_n$, see Equations (29) and (30),

$$\tau_n \sim 1.1 \times 10^{-1} Y^{-3} \exp(4.4 \times 10^9 \text{ K}/T) \left(\frac{T}{10^9 \text{ K}} \right)^3 \left(\frac{\rho}{10^5 \text{ g cm}^{-3}} \right)^{-2} \quad (49)$$

In order to estimate the horizontal propagation velocity across the NS, this velocity has to be multiplied by the factor $(2 - 3)R_{\text{Ro}}/H$ which expresses the ratio of the area of the burning front to the area of the vertical section of the ocean (see Landau & Lifshitz 1959). The horizontal velocity becomes

$$v_f \sim \sqrt{\frac{16\sigma_B}{3\tilde{c}_P} \frac{T^3}{\rho^2\tau_n} \frac{g}{H} \frac{1}{2\pi\nu\sqrt{\kappa_c}}} \quad (50)$$

or

$$v_f \sim 1.8 \times 10^6 Y^{3/2} \exp(-2.2 \times 10^9 \text{ K/T}) \text{ cm s}^{-1} \left(\frac{\nu}{450 \text{ Hz}}\right)^{-1} \left(\frac{\kappa_c}{0.07 \text{ cm}^2 \text{ g}^{-1}}\right)^{-1/2} \left(\frac{g}{2 \times 10^{14} \text{ cm s}^{-2}}\right)^{1/2} \left(\frac{H}{3 \times 10^2 \text{ cm}}\right)^{-1/2} \left(\frac{\tilde{c}_P}{10^8 \text{ erg g}^{-1} \text{ K}^{-1}}\right)^{-1/2} \quad (51)$$

Again, if $\tau_{\text{bar}} \sim \tau_{\text{cond}}$, then the actual $v_{f\perp}$ should be given by a combination of conduction and advection, with an extra term of the order of

$$\sqrt{\frac{D_{\perp\text{bar}}}{\tau_n}}. \quad (52)$$

to be included in equation (48). The result should then be multiplied by the same factor, $(2 - 3)R_{\text{Ro}}/H$.

The scaling expected from equation (51) agrees with what we measure in our simulations. The agreement is within half an order of magnitude and this allows us to put constraints on the numerical factors in front of equation (51) which are not determined by the order of magnitude estimates that led to it.

We verify the dependence of v_f on the spin rate ν using runs 6-10. In Fig. 9, we can see that increasing the rotation frequency slows down the flame, as expected, with a $1/\nu$ dependence. The dotted line in the upper panel shows the best linear fit to the data, which has a slope of $5.10 \times 10^7 \text{ cm s}^{-1}$ and an intercept of $8.25 \times 10^4 \text{ cm s}^{-1}$. The lower panel shows the relative difference between the fit and the results from the simulations.

The presence of the intercept at $1/\nu = 0$ is the most notable feature. This intercept is not predicted by the back of the envelope calculations leading to equation (51). Nonetheless, it is to be expected physically that even in the presence of extremely fast rotation, which would lead to a *vertical* interface, there should still be some conduction across the interface leading to a finite front speed.

By contrast, Fig. 10, where we plot v_f against the inverse heat conduction (our effective opacity κ_c), shows more complex behaviour. For opacities $\kappa_c \gtrsim 0.05 \text{ g cm}^{-2}$, the flame speed increases approximately with $1/\sqrt{\kappa_c}$ as expected from equation (51). Below it, the velocity seems to asymptote to $v_f \sim 1.99 \times 10^5 \text{ cm s}^{-1}$. In our simulations we see a change in the morphology of the flame: indeed all simulations showed a flame leaning on the hot-cold fluid interface similar to the middle right panel of Fig. 1, apart from simulation (9) ($\kappa_c = 0.001 \text{ g cm}^{-2}$), which does not show such a leaning flame and has a much more vertical structure of the temperature profile (Fig. 11), and simulation (8) ($\kappa_c = 0.01 \text{ g cm}^{-2}$) where this trend is beginning to become apparent.

We interpret this point as marking the transition where the conduction time scale τ_{cond} becomes comparable to the burning time scale τ_n and the thickness of the slanted burning front becomes comparable to the vertical scale height. At this point the front speed saturates and the whole layer burns through on the timescale τ_n : according to the original estimate of SLU (see the discussion leading to equations 21-23), this means that the horizontal speed saturates at $\sim R_{\text{Ro}}/\tau_n$. If we adopt the values $T = 6 \times 10^8 \text{ K}$ and

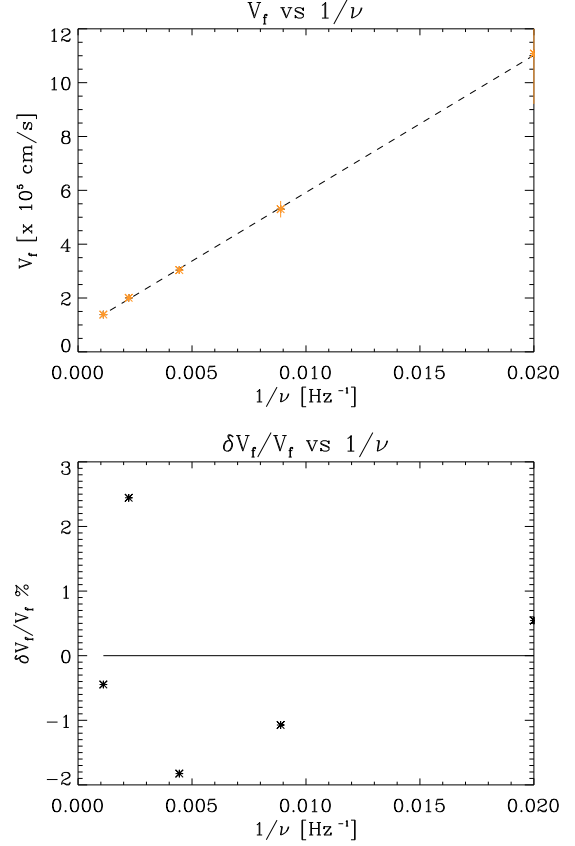


Figure 9. Upper panel: velocity of flame propagation versus $1/\nu$. Lower panel: residuals with respect to the best fit through the points versus $1/\nu$. All these runs have $\kappa_c = 0.07 \text{ cm}^2 \text{ g}^{-1}$.

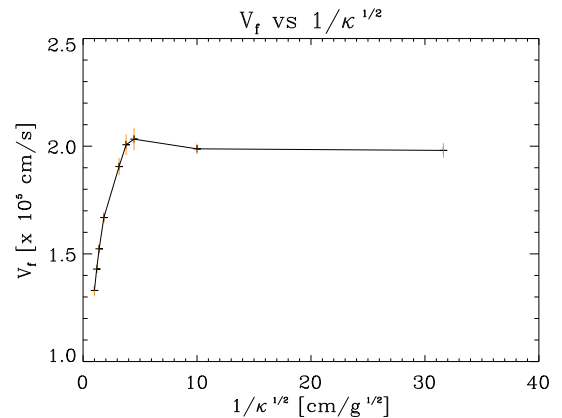


Figure 10. Velocity of flame propagation versus $1/\sqrt{\kappa_c}$. All these runs have $\nu = 450 \text{ Hz}$.

$\rho = 9 \times 10^5 \text{ g cm}^{-3}$, as in Table 2, we obtain an *average* burning rate of $\tau_n \sim 0.45 \text{ s}$, so that $2 R_{\text{Ro}}/\tau_n \sim 1.9 \times 10^5 \text{ cm s}^{-1}$. This order-of-magnitude estimate is in good agreement with what we measure.

On the other hand, when $\kappa_c \gtrsim 0.3 \text{ g cm}^{-2}$, we observe a greater deviation from our estimates. In this limit of small conductivity, we suspect that the baroclinic motions become more important. Their contributions, on top of those predicted by equation (51),

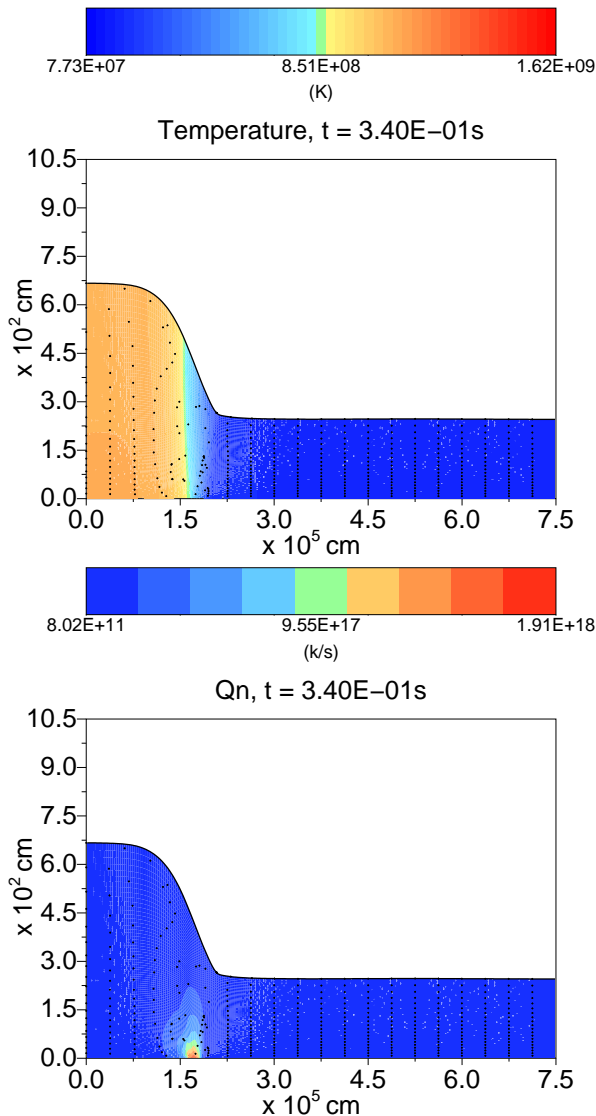


Figure 11. Temperature and reaction rate for simulation (9) after the flame is steadily propagating. The morphology of the flame is different from that shown in Fig. 1. This simulation shows the asymptotic behaviour seen in Fig. 10.

have to be taken into account, until the front speed asymptotes to a baroclinic-motion-driven system.

4 DISCUSSION AND CONCLUSIONS

In this paper, we have been able to simulate for the first time the lateral propagation of a *deflagrating* vertically resolved flame on the surface of an NS. We find that after an initial post-ignition adjustment, the front propagates steadily with constant velocity, until it reaches the opposite side of the simulation box. The fact that the flame velocity is constant (Fig. 6) gives us confidence that, regardless of the physics of the localized ignition, steady flame propagation depends only on the physics acting in the ocean layer and the conditions therein. After all the surface has been traversed by the flame, the fluid column cools down slowly, in a time which depends on the opacity (see Equation 37), whilst still burning the residual fuel. We note that in 2003, Anatoly Spitkovsky (unpublished)

obtained somewhat similar flame fronts using the `pencil` code. Due to computational constraints, however, he assumed unphysically large NS spins, so that the Rossby radius was comparable to the ocean scale height. The micro-physics of the flame propagation mechanism was not identified, and full exploration of the parameter range was not carried out (Spitkovsky, private communication).

We have explored the dependence of the flame speed on the spin frequency of the NS ν and the heat conductivity of the fluid (expressed as an inverse of the effective opacity κ_c). We measured velocities in the range $1.33 \times 10^5 - 1.11 \times 10^6 \text{ cm s}^{-1}$, which cross the entire domain of 7.5 km in 0.7 - 5.6 s. These numbers are in good agreement with the rise times observed from Type I burst sources, suggesting that we have included all the relevant physics in our simulations and that we are now in a position to explore in more detail the behaviour of flame propagation during Type I bursts. We caution the reader again from taking the speed values to be exact, given that our convergence tests suggest a somewhat slow convergence rate so that the true values will be slightly different; however, the conclusions are solid, especially the ones about the physical mechanism of flame spreading.

The flame propagates through a combination of the ageostrophic forward flow of the burning fluid on top of the as-yet unburnt fluid (as argued previously in SLU), and top-to-bottom heat transport across the large-area strongly-inclined interface between burning and cold fluid. Heat transport leading to ignition is affected primarily by microscopic heat conduction and, in runs where conductivity was set to lower values, by baroclinic motions.

In section 3.5 we derived an order of magnitude estimate for the velocity that the front would have if it were driven by conduction. We calculated a dependence of the speed on κ_c and ν of the form $1/\nu\sqrt{\kappa_c}$ (Figs 9 and 10) and confirmed these expectations with the results of our simulations. A breakdown of this κ_c dependence is seen at both low and high κ_c , which can be understood qualitatively. In particular, we observe the existence of a possible asymptote in the velocity when the effective opacity is too small, which we explain as follows. When the opacity decreases sufficiently, the conduction time scale becomes shorter than the nuclear burning time scale. The latter becomes the bottleneck, the burning front width becomes comparable to the scale height, and the nuclear burning time scale becomes the time scale of vertical expansion. This translates into a horizontal velocity of $\sim R_{Ro}/\tau_n$, as already anticipated by SLU.

There are a number of hydrodynamical issues that now have to be explored further. Firstly, the effect of the baroclinic instability at the hot-cold fluid interface could be explored in more detail. Secondly, the flow in the y -direction has a velocity comparable to the sound speed, and Kelvin-Helmholtz instabilities that might be generated by this flow need to be investigated. Other aspects of the flame propagation will be explored in future work, including the effects of a better burning prescription taking into account elements other than Helium. We also aim to investigate the possibility of exciting large-scale waves in the ocean, and the effect of magnetic fields.

Finally, some of our simulations suggest that in the absence of a sufficiently strong Coriolis force the flame will die out. This leads to an important question: can the flame cross the equator? Near the equatorial belt the effective Coriolis force is much weaker and this could lead to rapid lateral spreading of the burning front, and subsequent quenching of the burning by enhanced cooling. This would have important consequences for efforts to determine the NS radius from observations of type-I bursts (see, e.g., Steiner et al. 2010), since it is usually assumed that the whole star is

burning at the peak, and the derived radius of the burning area is used as a measure of the NS radius. If the flame cannot cross the equator, this fact has to be taken into account when dealing with those estimates. This would also have important implications for burst recurrence times, and may help to explain the properties of multi-peak bursts (Bhattacharyya & Strohmayer 2006). We plan to investigate this possibility by introducing a variable Coriolis parameter in future work, to simulate properly the changes that would occur as a flame approaches the equatorial belt.

Acknowledgements. We thank Frank Timmes for making his astrophysical routines publicly available. We also thank Anatoly Spitkovsky, Chris Matzner, Alexander Heger and Laurens Keek for useful discussions. We thank Simon Portegies Zwart for letting us use the LGM cluster (NWO grant no. 612.071.503) and Jeroen Bédorf for his help. This research was supported by NOVA and by internal grants from Leiden Observatory. Some of the research was carried out during an extended visit by YC to the School of Physics at Monash University, and he thanks the School for hospitality.

References

- Berkhout R. G., Levin Y., 2008, MNRAS, 385, 1029
 Bhattacharyya S., Strohmayer T. E., 2006, ApJ, 636, L121
 Braithwaite J., Cavecchi Y., 2012, MNRAS, 427, 3265
 Brown E. F., Bildsten L., 1998, ApJ, 496, 915
 Clayton D. D., 1984, Principles of stellar evolution and nucleosynthesis. The University of Chicago Press
 Cumming A., Bildsten L., 2000, ApJ, 544, 453
 Fryxell B. A., Woosley S. E., 1982a, ApJ, 258, 733
 Fryxell B. A., Woosley S. E., 1982b, ApJ, 261, 332
 Fujimoto M. Y., 1988, A&A, 198, 163
 Fujimoto M. Y., 1993, ApJ, 419, 768
 Fujimoto M. Y., Hanawa T., Miyaji S., 1981, ApJ, 247, 267
 Galloway D. K., Muno M. P., Hartman J. M., Psaltis D., Chakrabarty D., 2008, ApJS, 179, 360
 Heyl J. S., 2004, ApJ, 600, 939
 Inogamov N. A., Sunyaev R. A., 2010, Astronomy Letters, 36, 848
 Landau L. D., Lifshitz E. M., 1959, Fluid mechanics. Oxford: Pergamon Press
 Lewin W. H. G., van Paradijs J., Taam R. E., 1993, Space Science Reviews, 62, 223
 Lilly D., 1996, Atmospheric Research, 40, 143
 Malone C. M., Nonaka A., Almgren A. S., Bell J. B., Zingale M., 2011, ApJ, 728, 118
 Nozakura T., Ikeuchi S., Fujimoto M. Y., 1984, ApJ, 286, 221
 Ogura Y., Phillips N. A., 1962, Journal of Atmospheric Sciences, 19, 173
 Pedlosky J., 1987, Geophysical Fluid Dynamics. Springer-Verlag
 Piro A. L., Bildsten L., 2005, ApJ, 629, 438
 Press W. H., Teukolsky S. A., Vetterling W. T., Flannery B. P., 1992, Numerical recipes in FORTRAN. The art of scientific computing
 Shara M. M., 1982, ApJ, 261, 649
 Simonenko V. A., Gryaznykh D. A., Litvinenko I. A., Lykov V. A., Shushlebin A. N., 2012b, Astronomy Letters, 38, 305
 Simonenko V. A., Gryaznykh D. A., Litvinenko I. A., Lykov V. A., Shushlebin A. N., 2012a, Astronomy Letters, 38, 231
 Spitkovsky A., Levin Y., Ushomirsky G., 2002, ApJ, 566, 1018
 Steiner A. W., Lattimer J. M., Brown E. F., 2010, ApJ, 722, 33

- Strohmayer T. E., Zhang W., Swank J. H., Smale A., Titarchuk L., Day C., Lee U., 1996, ApJ, 469, L9+
 Timmes F. X., 2000, ApJ, 528, 913
 Timmes F. X., Swesty F. D., 2000, ApJS, 126, 501
 Watts A. L., 2012, ARA&A, 50, 609
 Zingale M., Timmes F. X., Fryxell B., Lamb D. Q., Olson K., Calder A. C., Dursi L. J., Ricker P., Rosner R., MacNeice P., Tufo H. M., 2001, ApJS, 133, 195

APPENDIX A: CONVERGENCE TESTS

In this appendix we show some of the convergence tests that were performed. We used resolutions of 60x24, 120x48, 240x96 and 480x192 to test the numerical properties of the code. We used the same values for the parameters as for reference run 6 (see Table 1).

First of all, we notice that the behaviour at different resolutions is qualitatively the same, showing the same initial transient phase and then stationary propagation (see Fig. A1), with particles moving along the interface due to the increased baroclinicity.

Secondly, we measure the convergence rate α according to

$$\alpha = \frac{\sum_{i,j} |T_{2,i,j} - T_{1,i,j}|}{\sum_{i,j} |T_{1,i,j} - T_{0.5,i,j}|}, \quad (\text{A1})$$

where the subscripts 2, 1, and 0.5 refer to the simulations with 120x48, 240x96 and 480x192; $i \in [1, 120]$ and $j \in [1, 48]$. The values of T for the higher resolution simulations are interpolated at the corresponding positions for the lowest resolution simulation. Since the timesteps are slightly different, we also needed to perform a linear interpolation in time. The results as a function of time are plotted in Fig. A2. This kind of convergence test is hampered by the fact that the flame speed is different and this gives high gradients at different spatial locations. Also, in increasing the resolution we are actually simulating different physics, since, for example, the convection that we can resolve is different: how to predict the effect of that on α is difficult and beyond the scope of this appendix. However, the fact that resolving more the convection cells has an effect on the convergence rate becomes apparent if we separate the domain in three horizontal domains: one from the left boundary up to the beginning of the flame (of the highest resolution simulation), one from the front of the flame (of the lowest resolution simulation) to the right boundary and one between these two. The first one, which is where we see the vertical convective cells, has a convergence rate lower than the average, while the second has a much better convergence rate. The middle one, which by construction does not encompass only the flame, has a convergence rate similar to the average one. The convergence rate using the simulations with 60x24, 120x48 and 240x96 is only slightly better.

If we measure a global quantity such as the velocity of the front, the results are: 3.43×10^5 , 2.48×10^5 , 2.01×10^5 and 1.67×10^5 cm s⁻¹. The convergence rate for the first three values is $\alpha = 2$, which basically implies linear convergence with the resolution, while it becomes $\alpha = 1.4$ when we consider the three simulations with higher resolution. If we were to fit a line through the first three values, the extrapolation for the ideal infinite resolution would be 1.54×10^5 cm s⁻¹ (see Fig. A3), while if we were to fit a non linear function of the kind $v = a + bh^\beta$, with $\beta = \log 1.4 / \log 2$, then the extrapolation would be 8.16×10^4 cm s⁻¹, which is still non-zero (Fig. A3). The real expected value for an infinitely resolved simulation should lie between those two. Finally, one very important aspect to point out is that the speed of the flame is *decreasing* with *increasing* resolution. This is a very

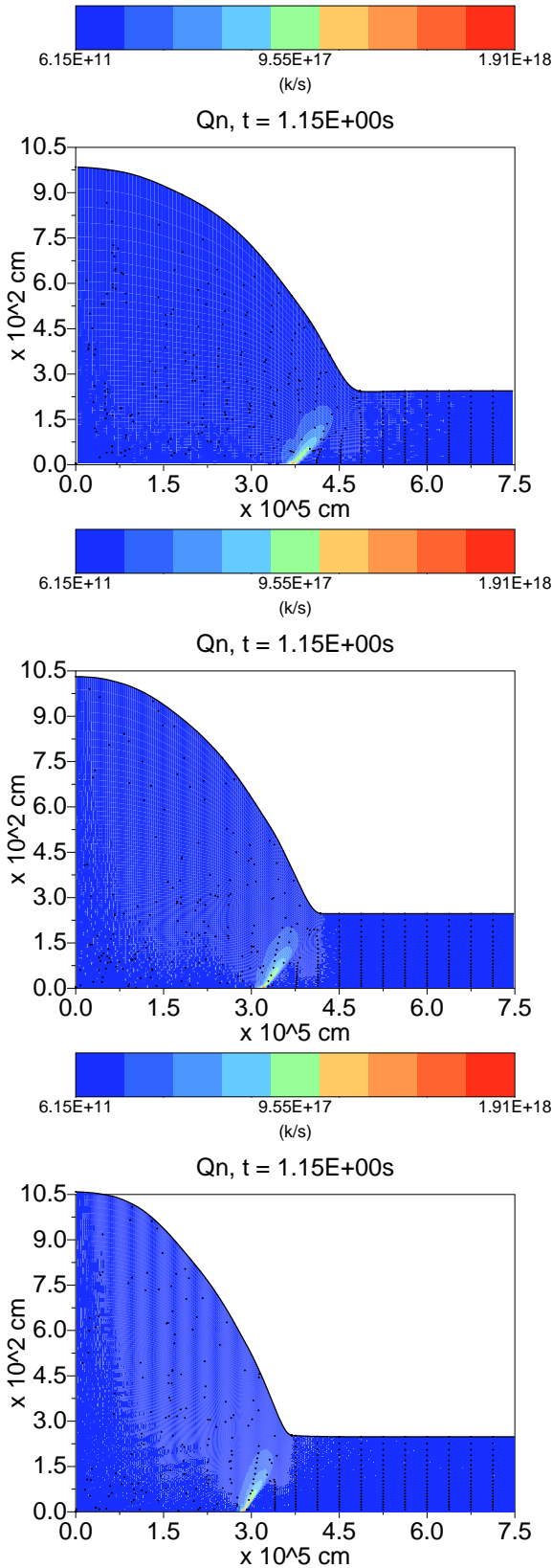


Figure A1. Snapshots of the burning rate for the simulations with resolutions 120x48, 240x96 and 480x192 at approximately the same time. The overall structure is the same, but the position of the flame is different due to the different values of the propagation speed. The different height of the fluid is just an artefact of the representation due to the different resolutions: we plot the centres of the grid cells and the higher the resolution the closer the centre of the top cell is to the physical top of the simulation.

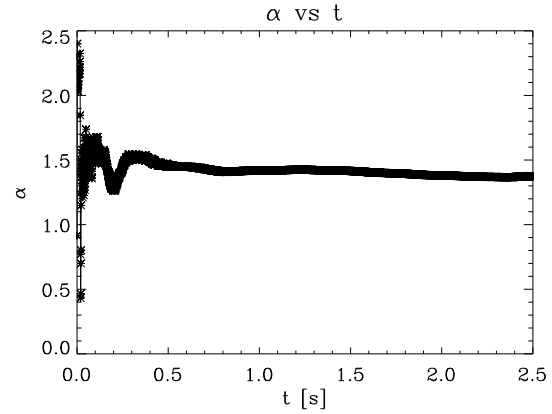


Figure A2. Convergence rate α (equation A1) for temperature as a function of time for the simulations with resolutions 240x96, 120x48 and 480x192. The convergence rate is hampered by the different velocities of the flame front. The comparison is carried out until the flame is present in all simulations.

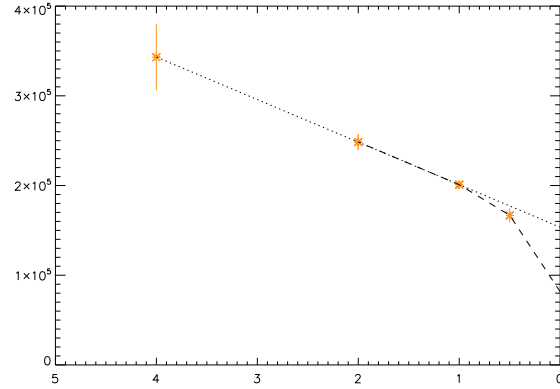


Figure A3. Flame spreading velocities as a function of grid spacing (simulation with 240x96 is the reference one). The dotted line indicates the linear fit and the dashed curve the non linear one. In both cases the velocity appears to be converging to a non-zero value, of at least $8.16 \times 10^4 \text{ cm s}^{-1}$.

good sign that the motion of particles we see should not develop into turbulence, hence possibly triggering a detonation.

Finally, measuring the independent residuals

$$I = \frac{\sum_{i,j} \left| \frac{[T_{i,j}(t+dt) - T_{i,j}(t)]/dt - \partial T_{i,j}/\partial t}{\partial T_{i,j}/\partial t} \right|}{m_x m_z} \quad (\text{A2})$$

where m_x and m_z are the resolutions in the horizontal and vertical directions, gives results that are at most 3×10^{-8} , so that they are never a problem.